RSC Advances

PAPER

View Article Online
View Journal | View Issue

Cite this: *RSC Adv.*, 2025, **15**, 3353

# Porphyrin-based porous organic polymer for the NIR-enhanced delivery of bupivacaine towards pain management in bacterial infection therapy†

Lichao Chu,‡[ab] Chunyu Dong,‡[c] Shuai Wang,[b] Xin Ding,[b] Jingsong Yuan,[b] Peilei Chen,[b] Yanhua Luo *[b] and Lingzhi Yu*[a]

Received 6th September 2024
Accepted 23rd December 2024

DOI: 10.1039/d4ra06433j

rsc.li/rsc-advances

Antibiotic-free strategies have gained widespread attention in combating bacterial infection-related wound therapy. Phototherapy is a precise treatment method that stands out from other therapeutic strategies. However, under the stimulus of local heat, patients might unconsciously touch the dressing at the infection sites, causing the dressing to fall off, thereby greatly diminishing the treatment effect. Therefore, pain management is quite essential in phototherapy. Herein, a porphyrin-based porous organic polymer (POP) with excellent photothermal capacities, denoted as P-POP, was developed as a carrier for the seamless integration of bupivacaine hydrochloride (BU), with both antibacterial and analgesic effects, to obtain a novel composite (P-POP-BU). The repetitive porphyrin units endowed excellent thermo-responsive properties to P-POP-BU, realizing the accelerated drug release following the local temperature increase triggered by laser illumination. P-POP-BU could realize the photo-enhanced BU release, enabling pain management during PTT. The antibacterial experiment demonstrated that the composite presented a synergistic and high-efficiency capacity to eradicate bacteria at the infection sites and significantly accelerate the repairing of wounds under laser irradiation. Notably, this special composite exhibited excellent biocompatibility with minimal side effects, making it a promising therapeutic platform for the light-triggered treatment of bacterial infections.

## Introduction

Open wound infection, especially those concerned with multi-drug resistant bacteria, is posing critical challenges to public health worldwide.[1–3] Currently, the most pervasive treatment method for bacterial infections is antibiotic therapy.[4] However, the unreasonable dosage and frequency lead to the emergence of drug-resistant bacteria, significantly diminishing the therapeutic effects, which further aggravates the difficulty of the treatment.[5–7] Antibiotic-free treatment options, which could effectively avoid drug resistance, have become the mainstream for sustainable development of biomedical technology.[8]

Phototherapy is an emerging nonpharmaceutical therapeutic method extensively investigated to combat drug-resistant strains and is currently undergoing various clinical trials.[9,10] Photothermal therapy is a popular method to fight against both Gram-positive (G+) and Gram-negative (G−) bacteria, effectively avoiding the emergence of drug-resistant bacteria.[11–13] In contrast to other therapies, PTT mainly depends on local photothermal conversion with the assistance of photothermal agents to kill bacteria. As an unpleasant feeling, pain, both acute and chronic, is one of the most common clinical symptoms, especially in trauma and disease conditions, which affects the normal life of patients.[14–16] Several people are suffering from numerous types of acute or chronic pain.[17] The clinical application of PTT would induce acute pain at the infection sites, causing conditioned reflexes.[18] Under painful stimuli, patients might involuntarily scratch the infected site, causing the dressing to fall off and thereby seriously affecting the treatment effect.[19] Hence, it is highly desired to manage the acute pain during PTT to achieve a high therapeutic effect while minimizing the unwanted side effects on the body.

Currently, local anesthetics are regarded as the most commonly used drugs for pain management in clinics.[20] Among the numerous anesthetics, bupivacaine hydrochloride (BU), with the inherent feature of no irritability to tissues, as well as a negligible effect on circulation and respiration, has been prevalently used in clinical treatment.[21] However, to maintain efficacy, it commonly requires frequent administration of small dosages of drugs, which not only brings pain to the patients but

---

[a] *Jinan Central Hospital, Shandong University, Jinan, Shandong, PR China. E-mail: pain-relief@163.com*

[b] *Weifang People's Hospital, Shandong Second Medical University, Weifang 261035, Shandong, PR China. E-mail: 55358645@qq.com*

[c] *Department of Neurointervention, Weihai Central Hospital Affiliated to Qingdao University, Weihai, Shandong, PR China*

† Electronic supplementary information (ESI) available: For the Experimental and Characterization methods, see the details in the ESI. See DOI: https://doi.org/10.1039/d4ra06433j

‡ These authors contribute equal to this work.

also causes toxic side effects due to blood concentration accumulation.[22] Therefore, it is highly desirable to develop a controllable or sustainable drug delivery system that could realize the on-demand anesthetic release and produce a local anesthetic effect.

Porous organic polymers (POPs) are synthetic multifunctional materials with custom-built structures and functions.[23–25] Currently, POPs have been used in, but not limited to, the fields of photo, electronic and biomedical science.[26–29] Noteworthily, POPs are constructed *via* organic building blocks connected with organic linkages, whose compositions are similar to biomacromolecules.[30] Thereby, POPs are frequently regarded as biocompatible multifunctional platforms for bacterial therapy, achieving the assembly of building blocks according to functional requirements.

Herein, an N-rich porphyrin-based POP, denoted as P-POP, was facilely prepared *via* the copolymerization of C8-symmetric triazine-porphyrin (Por) with C2-symmetric diformyl-salen-Fe (DSFe) through the acetal ammonia reaction.[31] P-POP featuring excellent photo activity could be used as the porous carrier for loading a painkiller (BU), which was loaded *via* the hydrogen bonding and van der Waals forces. Pain tests demonstrated that the final P-POP-BU composite could realize the near-infrared light (NIR)-enhanced drug release, achieving the on-demand release to the infection sites during the photothermal therapy, thereby obtaining the precise transdermal administration. The local temperature rise could dilate peripheral blood ducts in the delivery area, accelerating drug absorption through the blood ducts. As a result, P-POP-BU could not only manage the pain induced by local hyperthermia but also effectively kill the bacteria in the infected sites of the skin, significantly promoting the repairing of wounds. This therapeutic strategy provides a simple but high-efficiency and useful method for the concurrent management of acute pain and the repair of open wounds with bacterial infection.

## Results and discussions

As presented in Scheme 1, the photoresponsive porous organic polymer (P-POP) was prepared according to previous reports.[32] The local anesthetic was loaded into the porous network *via* physical agitation, in which the BU was firmly adsorbed into the porous skeleton through supramolecular interactions, including the hydrogen bond and van der Waals interactions with the N-rich porous polymer.[33] The drug loading capacity was determined by UV-Vis absorption by changing the mass ratio of P-POP to BU from 1 : 2 to 1 : 8. The corresponding results (Table S1†) demonstrated a stable drug loading capacity for P-POP. Increasing the mass ratio of POP to Bu from 1 : 2 to 1 : 8, the drug loading rate increased from 35.82% ± 0.73% to 70.79% ± 3.54%. But, the encapsulation rate reached a peak value of 35.81% ± 1.65% at the mass ratio of 1 : 4. Therefore, the P-POP-Bu composite specifically denoted the product obtained at the mass ratio of 1 : 4, which was utilized for subsequent experiments. The details for the synthesis of P-POP and P-POP-BU composite is given in the electronic ESI.†

To demonstrate the successful formation of the P-POP-BU composite, Fourier transform infrared spectroscopy (FTIR) and transmission electron microscopy (TEM) were concurrently conducted (Fig. 1).[34] Fig. 1a shows the FTIR spectra of P-POP collected before and after the loading of BU. As seen, the FTIR spectra P-POP-BU amalgamated the features of BU and P-POP concurrently, from which characteristic peaks of *sec*-ammonium (–N–H, 3415 cm$^{-1}$), imine (–C=N–, 1652 cm$^{-1}$) and methylidene (–CH$_2$–, 2981 cm$^{-1}$) belonging to the P-POP, as well as the enol formation (1685 cm$^{-1}$) assignable to the BU, could be clearly observed.[35–37] These results indicated the successful loading of BU into the P-POP networks. Fig. 1b and c present the TEM images of P-POP and P-POP-BU, respectively. As seen, P-POP displays an irregular bulk material morphology with intergrown macropores throughout the polymer skeleton. After the encapsulation of BU, the interconnected macropore was well maintained, indicating the excellent stability of P-POP as a drug carrier. Elemental mapping of P-POP-BU verified the co-existence of C, O, Fe, N and Cl, in which the Cl and O were ascribed to the BU (Fig. 1d).

Meanwhile, the solid-state CP-MAS $^{13}$C NMR spectra (solid state $^{13}$C NMR) were obtained to determine the carbon species in P-POP-BU (Fig. S2†). As observed, the solid-state $^{13}$C NMR signal was obscured by intense background signals, primarily due to the presence of paramagnetic Fe in P-POP-Bu. This paramagnetic Fe significantly interfered with both the external static magnetic field and the radio frequency field during the NMR experiment. However, the characteristic peaks in P-POP-Bu could still be found. The peaks at about 172.7 and 169.1 ppm corresponded to the C=N bond in the triazine units. The signal located at 129.5 ppm confirmed the presence of aromatic carbon in the benzene rings. The high field signals located at 28.8 and 15.2 ppm were assigned to the saturated carbons in the –CH$_2$– and –CH$_3$ groups of BU. All these consequences demonstrated the loading of Bu in the POP. The powder X-ray diffraction (XRD) pattern of P-POP-BU only displayed a strong broad diffraction peak ranging from 10 to 40°, indicating the amorphous structure of P-POP-BU (Fig. S3†). Meanwhile, the TG-DSC apparatus was used to illustrate the thermal behavior of P-POP-BU (Fig. S4†). As seen, the as-synthesized P-POP-BU possessed a relatively high thermal stability, with a tiny weight loss of less than 3% in the range of 20 to 100 °C, which was ascribed to the evaporation of water in the O, N rich high polarity skeleton. Such a consequence showed the application potential of P-POP-BU as a photothermal agent. The remaining weight was well retained above 50% even at 800 °C.

The low-temperature N$_2$ adsorption and desorption measurements were conducted on P-POP and P-POP-BU to explore the change in porosity after the encapsulation of BU. As seen from Fig. S5,† both samples exhibited type III adsorption curves with a significant hysteresis loop appearing at the branch of the uptake isotherms, suggesting the mesopore and macropore-dominated pore structure. The unique pore structure was beneficial for the release of drugs under external stimulations. The BET surface area was calculated to be 92.3 m$^2$ g$^{-1}$ for P-POP, which was higher than that for P-POP-BU (16.5

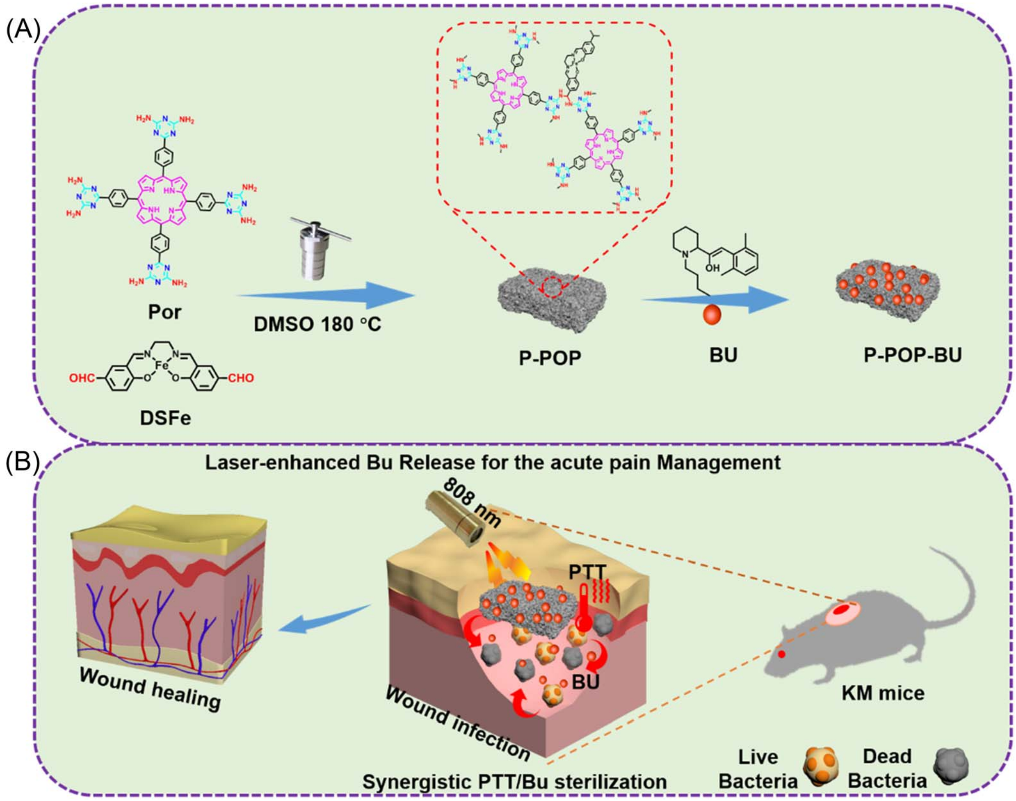

Scheme 1 (A) Schematic of the synthesis of P-POP, as well as the corresponding P-POP-BU composite. (B) The photo-controllable BU delivery for pain management and the synergistic photothermal/photodynamic/BU sterilization to accelerate the restoration of infected wounds.

$m^2$ $g^{-1}$), further confirming the loading of BU. Further analysis of the pore size distribution (PSD) also demonstrated the mesopore and macropore-dominated pore structure for both samples (Fig. S6†). Notably, mesopores were still retained in P-POP-BU despite partially blocked pores. Then, the hydrolytic and enzymatic degradation behavior, along with pH changes, were investigated. Initially, the pH stability test was conducted by recording the changes in UV-visible absorption with pH (Fig. S7a†). As seen, the UV-visible absorption curves of P-POP remained unchanged as the pH decreased from 7.4 to 2.5. However, new absorption peaks ascribed to the degradation of P-POP appeared with the continuous increase in acidity to pH 1.5. Meanwhile, the enzyme degradation behavior of P-POP was also conducted under $^{\bullet}$OH-environment at the pH of 3.5 (Fig. S7b†). Notably, after a duration of 30 min, P-POP only underwent partial degradation when exposed to 1× concentration of $^{\bullet}$OH. However, significant degradation of P-POP was evident when the concentration of $^{\bullet}$OH was increased to 10×. However, in practical wound trauma-sensitive application environments, both the pH levels and $^{\bullet}$OH concentrations were generally not as extreme as those used in experimental conditions. Therefore, P-POP is an outstanding choice as a BU carrier.

Then, the photophysical performance of P-POP-BU was estimated using pure water as the control sample. As shown in Fig. 2a, under the NIR illumination (808 nm, 1.5 W $cm^{-2}$ for 10 min), P-POP-BU presented a sample dosage-dependent warming behavior, which was significantly increased with the rise in sample concentrations.[38] Specifically, with the extension of irradiation time, the temperature of aqueous dispersion increased rapidly to the equilibrium temperature within 10 min (Fig. 2a). The equilibrium temperature increased from 31.5 to 54.6 °C with the sample concentration rising from 50 to 600 μg $mL^{-1}$. In contrast, the temperature of pure water barely changed under the same conditions. The temperature change ($\Delta T$) was calculated to be 5.0, 12.4, 17.5, 22.9, and 27.4 °C at concentrations of 50, 100, 200, 400, and 600 μg $mL^{-1}$, respectively. Noteworthily, the temperature of the aqueous dispersion reached 50.8 °C at the P-POP-BU dosage of 400 μg $mL^{-1}$ (Fig. 2a), which was sufficient to kill bacteria by the local photothermal effect. Meanwhile, as shown in Fig. 2c, the heating performance of P-POP-BU was also positively correlated with the laser power intensities.[39] After 10 min of laser irradiation, the final temperatures of the dispersion were determined to be 45.1, 50.8 and 55.6 °C at the laser powers of 1.0, 1.5 and 2.0 W $cm^{-2}$, respectively. These results indicated that P-POP-BU could effectively convert the NIR into localized heat to combat bacterial infection. Subsequently, the photothermal conversion stability of P-POP-BU was evaluated by three consecutive laser on/off cycles. As shown in Fig. 2d, the temperature fluctuation during the three consecutive cyclic heating processes was negligible, indicating the good photothermal stability of the P-POP-BU composite.[40] In addition, the photothermal conversion efficiency ($\eta$) was investigated based on a single switching cycle (Fig. 2f). The $\eta$ value calculated according to eqn (S1) to (S3)†

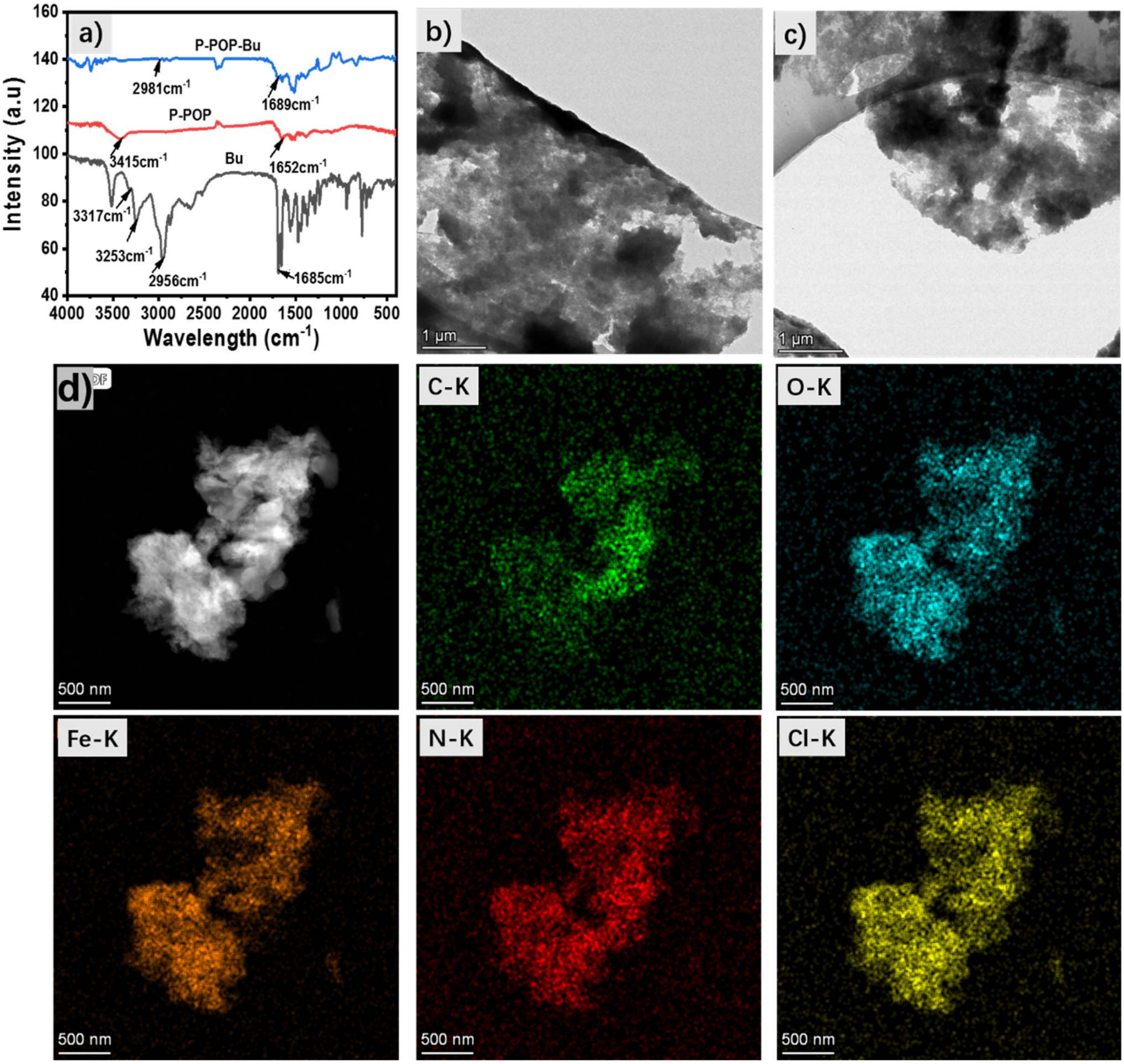

Fig. 1 Physical characterization of P-POP and P-POP-BU: (a) FTIR of P-POP and P-POP-BU; (b) TEM of P-POP; (c) TEM of P-POP-BU; (d) elemental mapping images (C, O, Fe, N, and Cl) of P-POP-BU.

was estimated to be 47.64% based on the heat transfer time constant (Fig. 2g) and the temperature change in a single cycle. These results indicated that P-POP-BU also featured excellent photothermal properties, which was suitable for application in NIR-induced photothermal therapy.

Then, the pain management performance was estimated *via* the analgesic effect on mice by subcutaneous administration. The pain management effect was reflected in the duration of effective analgesia recorded for different administration groups. As seen from Videos 1 and 2 given in the ESI,† due to the photo responsiveness of the P-POP-BU, in the exertion of NIR irradiation (2 min), no paw withdrawal response was detected. This result showed the P-POP-BU could realize the NIR-controlled drug release, which is highly desirable for clinical applications. Meanwhile, the continuous analgesic duration of the released drug was tested in a 12 h cycle. The corresponding results demonstrated the analgesic duration gradually decreased with the increasing cycle numbers. The analgesic duration of the P-POP-BU + NIR group changed from 51 ± 2.76 to 15.3 ± 3.27 (min) after four cycles (Fig. S1†).

The *in vitro* bacteriostatic activity of P-POP-BU was investigated *via* the plate counting method using the P-POP sample as the control. In order to investigate the *in vitro* antimicrobial ability of P-POP before and after loading BU, the inhibitory ability of P-POP-BU against *S. aureus* and *E. coli* was first evaluated by the plate counting method.[41] As seen in Fig. 3, the

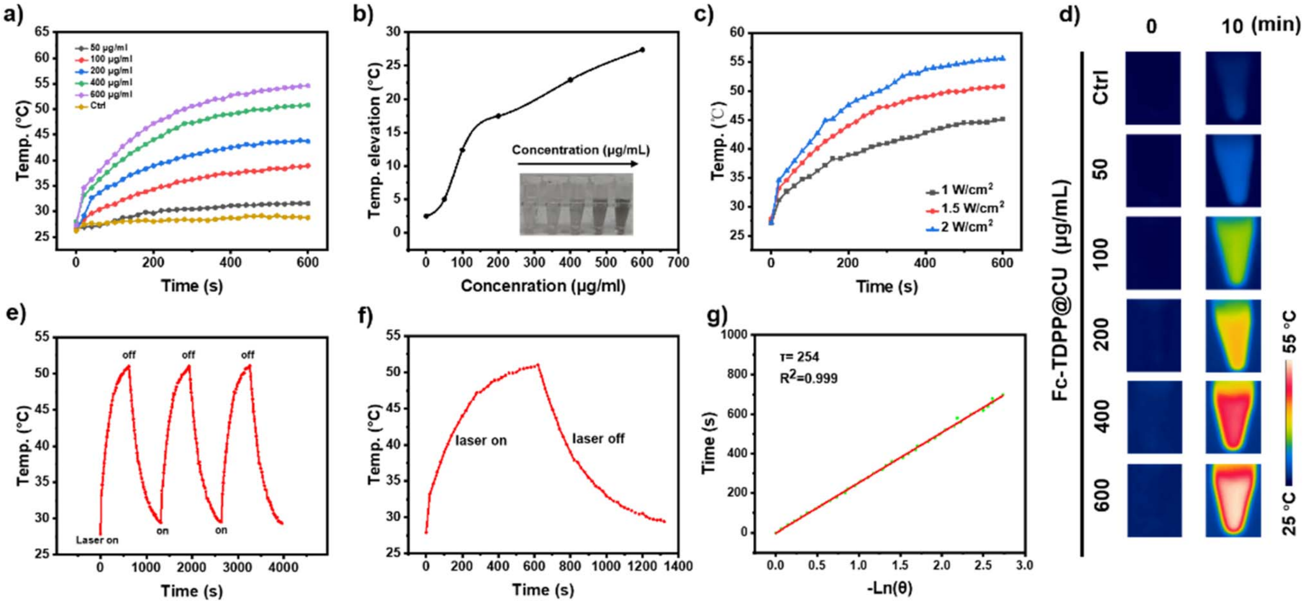

Fig. 2 (a) Temperature curves of P-POP-BU aqueous dispersions at varied concentrations under red light (808 nm, 1.5 W cm$^{-2}$ for 10 min) irradiation; (b) plot of temperature change *vs.* the concentration of P-POP-BU after exposure to red light. Inset: photograph of the P-POP-BU aqueous dispersion; (c) temperature rising curves of P-POP-BU (400 μg mL$^{-1}$) under different powers of laser irradiation; (d) corresponding infrared thermal images of P-POP-BU aqueous dispersions with different concentrations; (e) temperature change curve of aqueous dispersion of P-POP-BU (400 μg mL$^{-1}$) over three laser irradiation on/off cycles; temperature change curve (f) *versus* negative natural logarithm of cooling time and temperature (g) for aqueous dispersion of P-POP-BU (400 μg mL$^{-1}$) under red light ($\lambda$ = 808 nm, 1.5 W cm$^{-2}$) illumination in a single on/off.

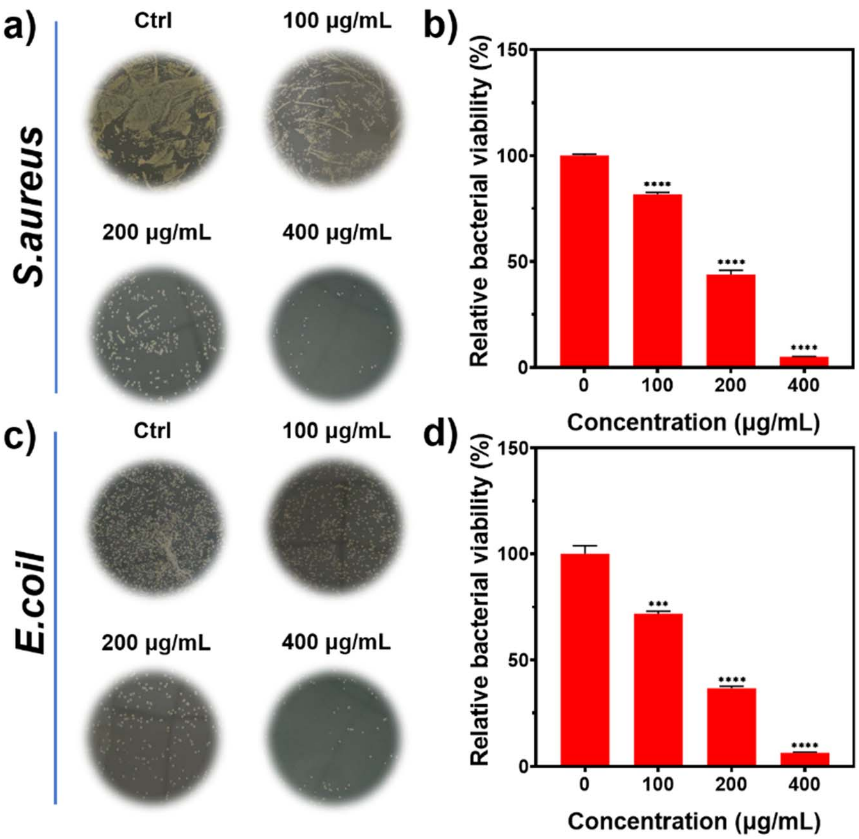

Fig. 3 Pictures of colonies of *S. aureus* and *E. coli* after co-culture with (a) *S. aureus* and (c) *E. coli* for 12 h using different concentrations of P-POP-BU treated with an 808 nm red light (1.5 W cm$^{-2}$, 10 min). (b and d) Corresponding cell viability graphs of *S. aureus* and *E. coli* determined by the plate counting method, respectively.

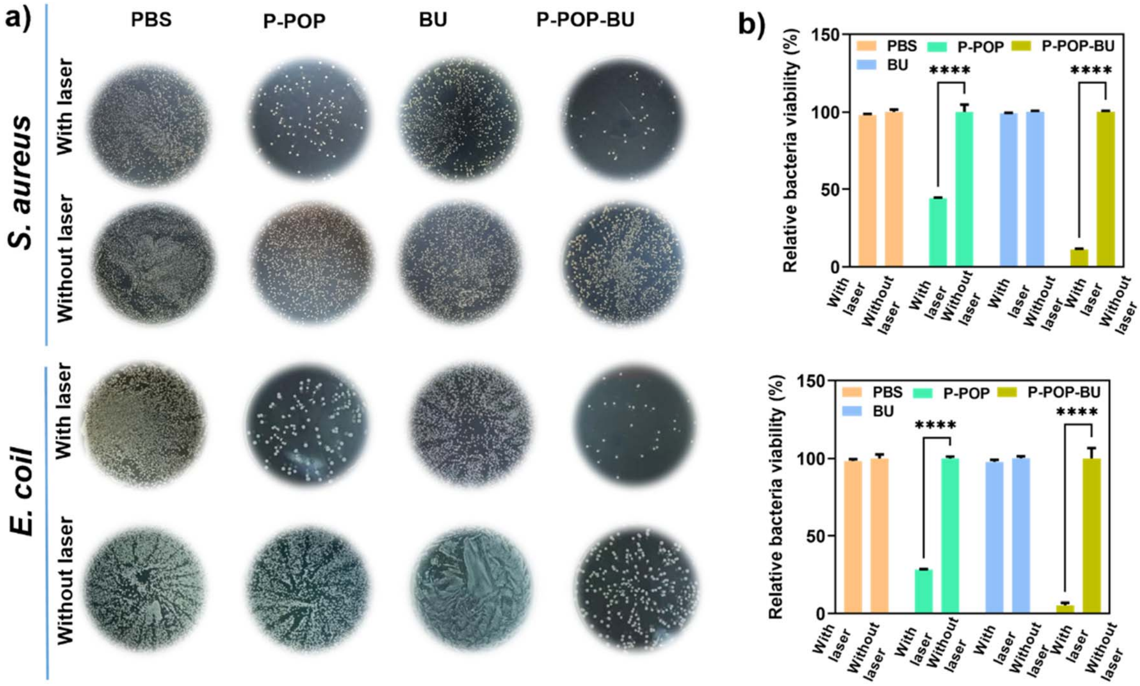

Fig. 4 Photographs of bacterial colonies formed by (a) *S. aureus* and *E. coli* treated with PBS, PBS + laser, P-POP + laser, BU, BU + laser, P-POP-BU and P-POP-BU + laser based on the plate count method (concentration: 400 μg mL$^{-1}$); corresponding bacterial viabilities of (b) *S. aureus* and *E. coli* treated with PBS, PBS + laser, P-POP + laser, BU, BU + laser, P-POP-BU and P-POP-BU + laser, and the laser was set at the wavelength of 808 nm (1.5 W cm$^{-2}$, 10 min).

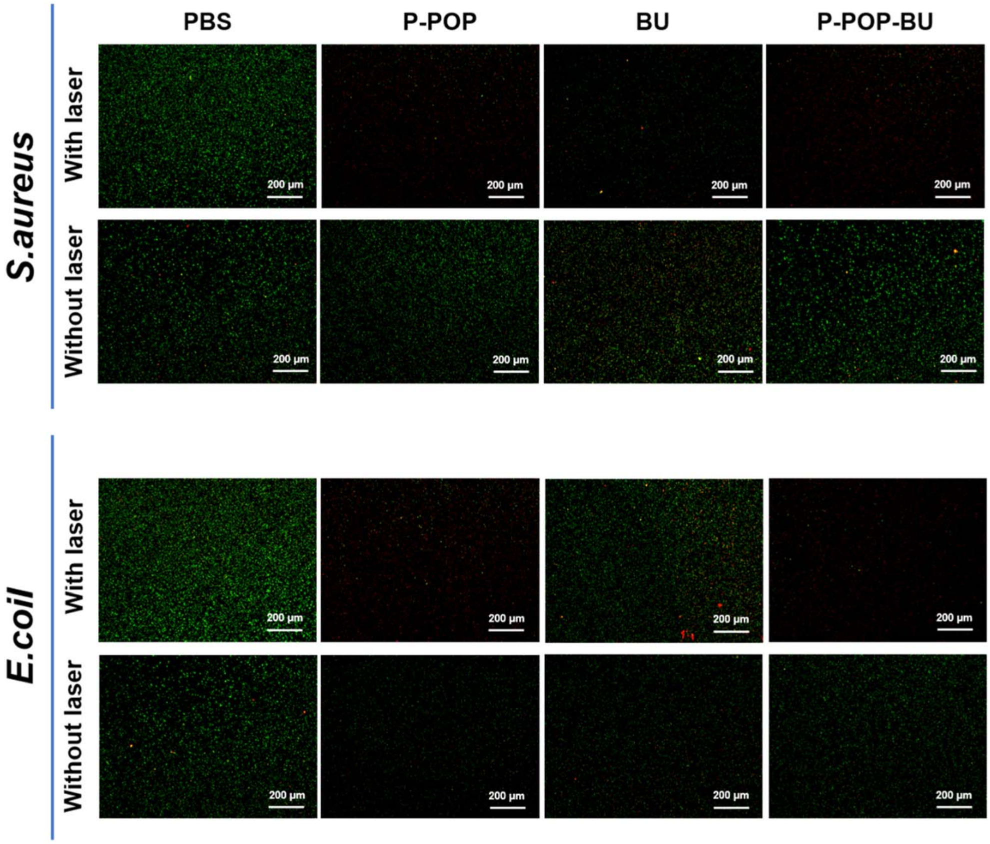

Fig. 5 Fluorescence images of *S. aureus* and *E. coli* incubated with PBS + laser, P-POP + laser and P-POP-BU + laser DMAO and EthD-III co-stained (concentration: 400 μg mL; scale bar = 200 μm, irradiation time = 1.5 W cm$^{-2}$, 10 min).

bactericidal ability of P-POP-BU against *S. aureus* and *E. coli* was greatly enhanced with increased sample dosage under 808 nm laser irradiation (1.5 W cm$^{-2}$, 10 min). At a concentration of 100 μg mL$^{-1}$, the bacterial survival rates of *S. aureus* and *E. coli* were determined to be 81.67% ± 1.00% and 71.91% ± 1.12%, respectively. With the dosage increased to 200 μg mL$^{-1}$, the survival rates decreased to 47.2% ± 1.04% and 43.7% ± 0.89% for *S. aureus* and *E. coli*, respectively. When the concentration was increased to 400 μg mL$^{-1}$, the bacterial survival rates reached 5.07% ± 0.21% and 6.29% ± 0.38% for *S. aureus* and *E. coli*, respectively.

To illustrate the sterilization mechanism, both the *S. aureus* and *E. coli* were treated with P-POP and P-POP-BU, respectively, using PBS and BU as the control group (Ctrl). As seen in Fig. 4, after 12 h of co-culture, different bacterial strains treated with PBS and BU presented similar antibacterial effects regardless of laser irradiation; the number of living *S. aureus* and *E. coli* treated by P-POP and P-POP-BU at the sample concentration of 400 μg mL$^{-1}$ under the laser illumination (808 nm, 1.5 W cm$^{-2}$, 10 min) sharply decreased and were much higher in the corresponding samples without laser irradiation. Specifically, both the *S. aureus* and *E. coli* treated by PBS and BU presented roughly the same number of colonies regardless of the laser irradiation, which hardly caused any damage to the bacteria. By contrast, both the P-POP + Laser and P-POP-BU + laser groups presented much stronger antibacterial effects than the P-POP and P-POP-BU groups. For example, the bacterial survival rates of *S. aureus* and *E. coli* in the P-POP + laser group were determined to be 5.56% ± 0.23% and 6.64% ± 0.56%, respectively. In comparison, the survival rate of *S. aureus* and *E. coli* in the P-POP-BU + laser group treatment decreased to 1.12% ± 0.09% and 1.73% ± 0.74%, respectively. This was due to the synergistic effect of the bactericidal properties of bupivacaine hydrochloride and the N–H-rich porous skeleton, in which the BU could protonate the porous skeleton, enhancing the adhesion with bacteria and achieving an additional effect.[41]

To further confirm the damaging effect of P-POP-BU on bacteria, fluorescence microscopy was performed using DMAO/EthD-III straining, in which the live bacteria with intact membranes could only be stained by DMAO with green fluorescence, and the dead bacteria could be stained with EthD-III with red fluorescence.[42,43] As seen in Fig. 5, the results of live/dead staining were consistent with those of the aforementioned results; both bacteria under different treatments showed varied fluorescence signals. For example, the bacteria treated with the PBS and PBS + laser groups showed only strong green fluorescence. Owing to the intrinsic antibacterial action of BU, both red and green fluorescence was detected for the bacteria treated by BU and BU + laser groups. However, the bacteria under the treatment of P-POP + laser and P-POP-BU + laser groups presented a much stronger red fluorescence than those treated by P-POP and P-POP-BU. Almost all the bacteria were

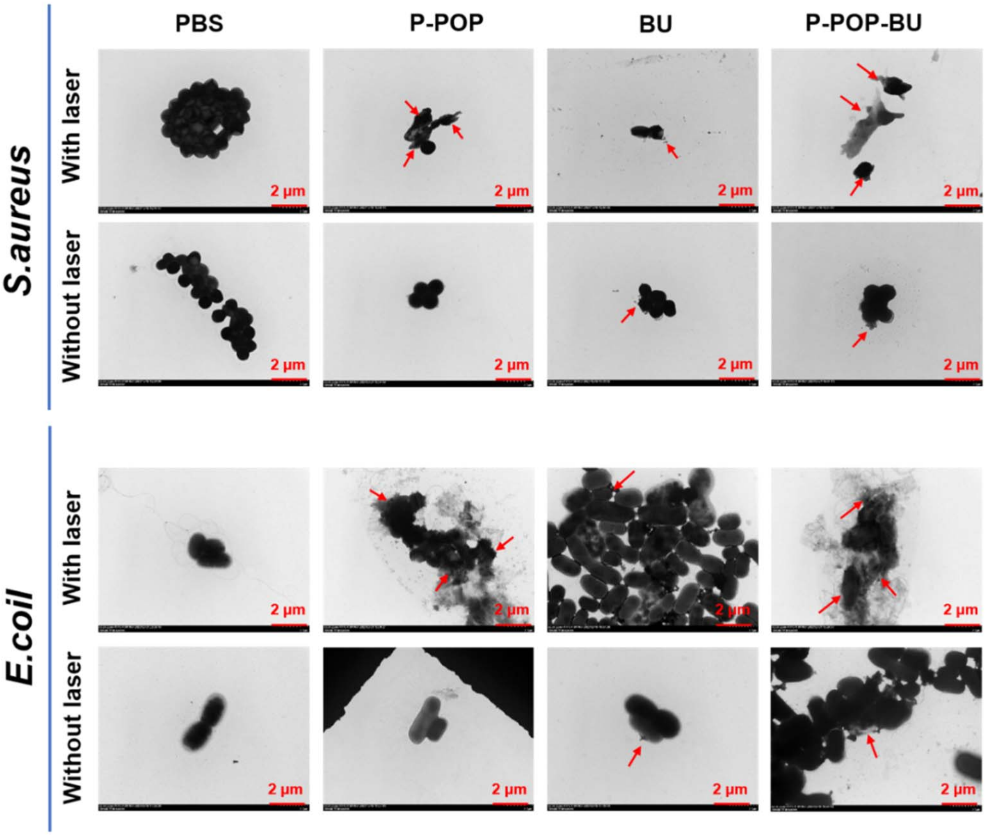

Fig. 6 TEM images of *S. aureus* and *E. coli* incubated with PBS + laser, P-POP + laser and P-POP-BU + laser. The red tip in the picture represents the location of the injury (400 μg mL; scale bar = 2 μm, irradiation time = 1.5 W cm$^{-2}$, 10 min).

labelled with red fluorescence after co-culture with P-POP + laser and P-POP-BU + laser for 24 h. These results further demonstrated the advantages of P-POP-BU in the antibacterial therapy.

In addition, the integrity of the bacterial membranes under different treatments was directly observed by TEM (Fig. 6).[44] As seen in the PBS and PBS + laser groups, the bacterial membranes of *S. aureus* and *E. coli* were all well-retained intact with smooth surfaces, indicating the viability of bacteria was not affected by the NIR laser irradiation. Similar to the live/dead staining results, the morphology of bacterial membranes treated by the P-POP + laser group and the P-POP-BU + laser group were extensively damaged with the leakage of cellular contents. Therefore, P-POP-BU with photo-triggered antimicrobial capacity possessed great application potential as a broad-spectrum antibiotic-free antimicrobial agent with high bacterial killing efficiency.

Inspired by the satisfying *in vitro* antibacterial ability of as-synthesized samples, the *in vivo* assay was also conducted to estimate the real application potential of P-POP-BU. The animal experiments were performed in strict accordance with the ethical norms of the Ethics Committee of Shandong University. The mice with back *S. aureus*-infection models were treated with different therapy schedules, including (I) control, (II) BU, (III) P-

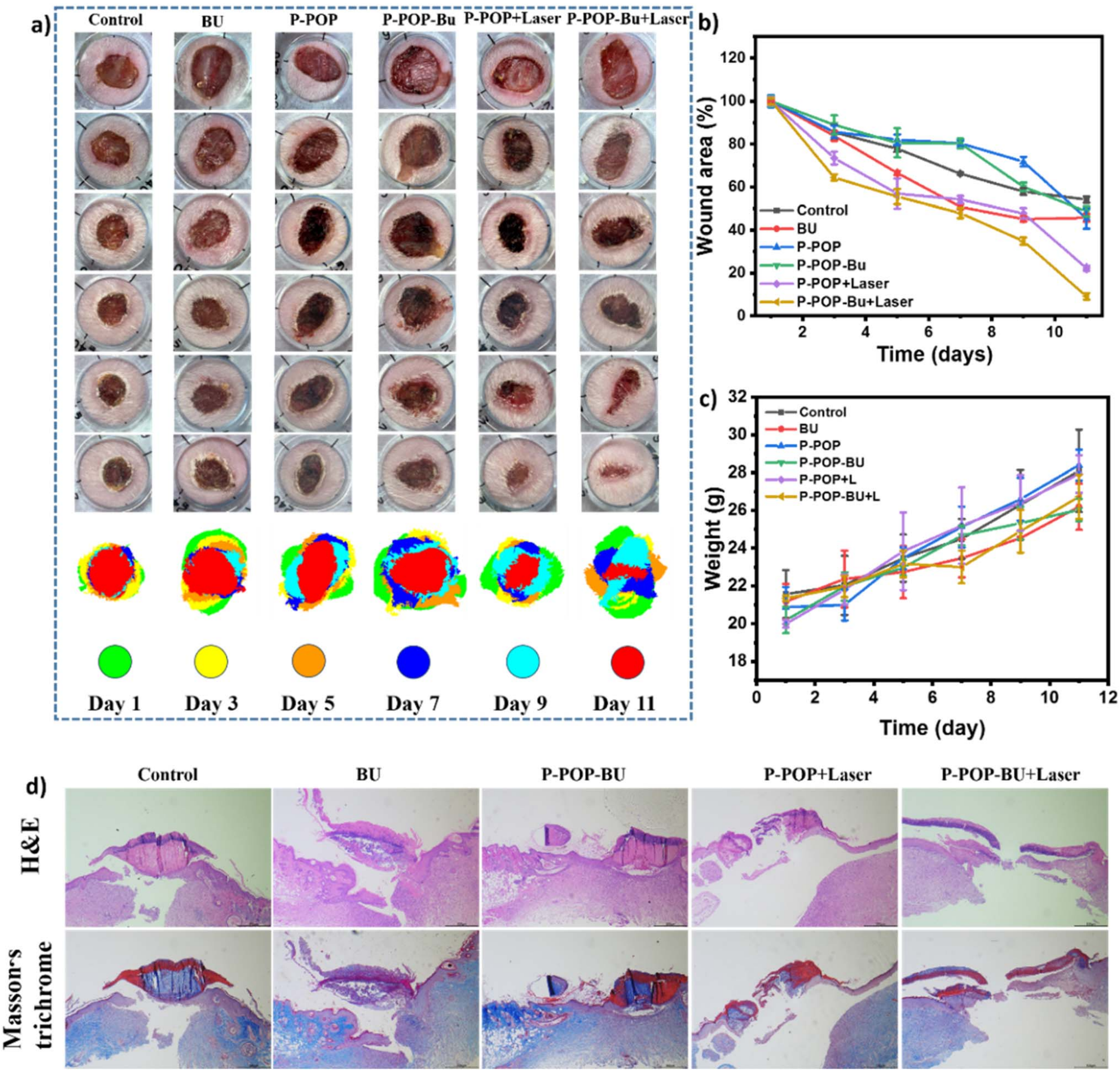

Fig. 7 Evaluation of the therapeutic efficacy of P-POP-BU in combating bacterial infection and accelerating the restoration of open wounds. (a) Images capturing wounds and wound trace simulation results of regenerated skin under varied treatment groups on days 0, 1, 3, 5, 7, 9, and 11. (b) Quantified analysis results of wound areas in various treatment groups. (c) Body weight change of mice under various treatments. (d) Histological analysis of the regenerated skin tissue on day 11 at the wound sites *via* the H&E staining and Masson's trichrome staining, scale bar = 100 μm.

POP, (IV) P-POP-Bu, (V) P-POP + laser, and (VI) P-POP-BU + laser groups, respectively.[45] Animal experiments were conducted on day 0 for model construction and inoculated with *S. aureus*. As shown in Fig. 7, the treatment was carried out on days 1 and 3. The wound healing and body weights were recorded on days 1, 3, 5, 7, 9, and 11, respectively. As shown in Fig. 7a, all wounds were visibly infected, and the wounds appeared pus-filled prior to treatment on day 1. One could see clearly that all the wounds gradually healed as the treatment progressed, but different groups presented varied healing degrees. In the first 5 days, all wounds in different treatment groups were crusted. The differences in treatments could be clearly seen on day 7. As seen, the trauma area of mice treated by the P-POP-BU + laser group was significantly smaller than that treated by other

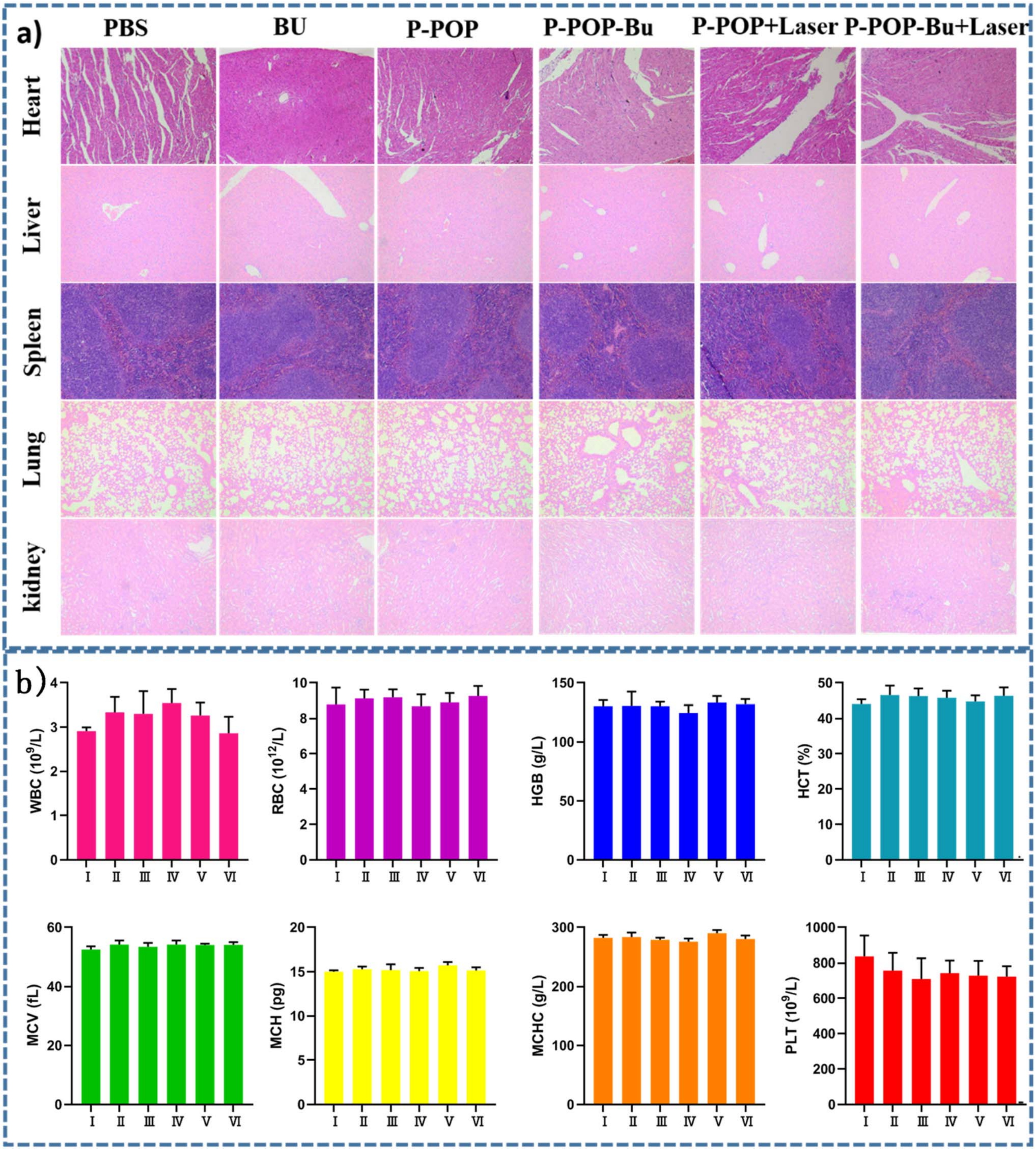

Fig. 8 (a) H&E staining on the major organs of mice following various treatments. (b) Biochemical indexes of mice obtained from the routine blood tests while undergoing different treatments.

groups. After day 11, the wound areas under the treatment of P-POP + laser and P-POP-BU + laser groups were smaller than those treated by the other groups. The wound area of mice was quantified *via* the calculation of the healing rate of wounds. As displayed in Fig. 7b, the wound healing rates of mice treated by (I) control, (II) BU, (III) P-POP, (IV) P-POP-BU, (V) P-POP + laser, and (VI) P-POP-BU + laser were determined to be 46.0%, 54.3%, 54.6%, 51.4%, 77.8%, and 90.8%, respectively. These results indicated that P-POP-BU + laser possessed a significant inhibitory effect on the bacteria in traumatically infected wounds, thereby accelerating the repair of infectious wounds. Meanwhile, the body weights of the mice (Fig. 7c) fluctuated within the normal physiological range during the 11 day treatments, indicating the negligible toxicity of P-POP-BU on the growth of mice during the treatment.[46]

Additionally, histological examination was performed on the *S. aureus*-infected wounds using hematoxylin & eosin (H&E) staining and Masson trichrome staining, concurrently. As shown in Fig. 7d, after the 11 day treatment, significant inflammatory cell infiltration was observed in the H&E tissue staining of regenerated skin treated by Control, BU, P-POP, as well as P-POP-BU groups. In contrast, the skin of mice treated by the P-POP + laser and P-POP-BU + laser groups displayed pronounced neovascularization and fibroblasts. Compared with P-POP + laser, the mice under the treatment of P-POP-BU + laser presented much more neovascularization and glands. Such consequences demonstrated that P-POP-BU + laser could significantly accelerate the restoration of infectious wounds.

As a fundamental requisite for the real application of a therapeutic agent, the *in vivo* biocompatibility of P-POP-BU was also estimated.[47] First, the H&E staining was performed to assess the lesions on the major organs of mice (heart, liver, spleen, lung, and kidneys) following various treatments. As shown in Fig. 8a, similar to the PBS group, no significant morphological damage or discernible inflammation could be detected from the H&E staining of the major organs of mice (Fig. 8a) by the treatment of other groups. Therefore, P-POP-BU could act as a smart therapeutic platform with high antimicrobial activity and biosafety concurrently, featuring great potential in the field of biological wound reconstruction.[48] Furthermore, the blood samples were respectively collected from mice under various treatments after the whole treatment for the routine blood tests. As shown in Fig. 8b, the relevant biochemical indices were all similar to those treated by PBS (blank group), which was within the normal ranges, further demonstrating a favorable *in vivo* blood biocompatibility of as-synthesized P-POP-BU.[49] Meanwhile, the hemolysis (Fig. S8a†) and cytotoxicity assay (Fig. S8b†) were conducted to assess the *in vitro* biocompatibility of P-POP-BU. Notably, the hemolysis rate remained safely within the acceptable limits across the experimental concentration range, with no hemolysis observed even at a high concentration of P-POP-BU of 500 μg $mL^{-1}$. Furthermore, *in vitro* cellular assessments employing 3T3 cells as models indicated that P-POP-BU exhibited non-toxic properties towards normal cells, maintaining cell viability of over 80% at a concentration of 500 μg $mL^{-1}$. Collectively, all these findings underscored the insignificant systemic toxicity of P-POP-BU, positioning it as a promising non-toxic therapeutic agent for dual applications in pain management and bacterial inactivation.

## Conclusion

Herein, a simple and straightforward method was introduced for the fabrication of multifunctional physical antibacterial agents with pain management capabilities to combat bacterial infections. The unique composite, designated as P-POP-BU, harbored remarkable photothermal properties and photoinduced drug release capacities and was synthesized *via* the loading of BU into the porous polymer skeleton (P-POP) through the supermolecular forces (hydrogen bonding and porous adsorption). P-POP was obtained *via* the copolymerization of porphyrin units containing multiple amino groups with diformaldehyde-salen-Fe. The resulting composite, P-POP-BU, could function as a photo-controlled drug delivery system, simultaneously achieving synergistic antibacterial and on-demand pain management. Notably, both *in vitro* and *in vivo* antibacterial experiments confirm that the P-POP-BU composite displayed a synergistic and highly efficient capacity to eliminate bacteria at infection sites, significantly accelerating wound healing under laser irradiation. This study presents a versatile approach for crafting specialized therapeutic agents as promising therapeutic platforms for light-triggered bacterial infection treatment and wound healing promotion.

## Data availability

The authors declare that all the experimental data are available from the corresponding authors upon reasonable request.

## Conflicts of interest

There are no conflicts to declare.

## Acknowledgements

This work was supported by the Weifang City health Commission project (WFWSJK-2023-232); Science and Technology Support Plan for Youth Innovation in Universities of Shandong Province (2022KJ264).

## References

1 M. C. Nolff, S. Reese, M. Fehr, R. Dening and A. Meyer-Lindenberg, Assessment of wound bioburden and prevalence of multi-drug resistant bacteria during open wound management, *J. Small Anim. Pract.*, 2016, **57**(5), 255–259.

2 M. G. Rippon, A. A. Rogers and S. Westgate, Treating drug-resistant wound pathogens with non-medicated dressings: an in vitro study, *J. Wound Care*, 2019, **28**(9), 629–638.

3 X. Yan, J. F. Song, L. Zhang and X. Li, Analysis of risk factors for multidrug-resistant organisms in diabetic foot infection, *BMC Endocr. Disord.*, 2022, **22**(1), 46.

4 L. J. Bessa, P. Fazii, M. Di Giulio and L. Cellini, Bacterial isolates from infected wounds and their antibiotic susceptibility pattern: some remarks about wound infection, *Int. Wound J.*, 2015, **12**(1), 47–52.

5 X. Wang, X. Sun, T. Bu, Q. Wang, P. Jia, M. Dong and L. Wang, In situ fabrication of metal-organic framework derived hybrid nanozymes for enhanced nanozyme-photothermal therapy of bacteria-infected wounds, *Composites, Part B*, 2022, **229**, 109465.

6 X. Yu, J. Zhao and D. Fan, A dissolving microneedle patch for antibiotic/enzymolysis/photothermal triple therapy against bacteria and their biofilms, *Chem. Eng. J.*, 2022, **437**, 135475.

7 G. Li, Z. Lai and A. Shan, Advances of Antimicrobial Peptide-Based Biomaterials for the Treatment of Bacterial Infections, *Adv. Sci.*, 2023, **10**(11), 2206602.

8 Y. Wang, Y. Yang, Y. Shi, H. Song and C. Yu, Antibiotic-free antibacterial strategies enabled by nanomaterials: progress and perspectives, *Adv. Mater.*, 2020, **32**(18), 1904106.

9 G. Wei, G. Yang, Y. Wang, H. Jiang, Y. Fu, G. Yue and R. Ju, Phototherapy-based combination strategies for bacterial infection treatment, *Theranostics*, 2020, **10**(26), 12241.

10 Y. Kong, Q. Jiang, F. Zhang and Y. Yang, Small molecular fluorescent probes: application progress of specific bacteria detection and antibacterial phototherapy, *Chem.–Asian J.*, 2023, **18**(11), e202300178.

11 F. Li, K. Huang, H. Chang, Y. Liang, J. Zhao, S. Yang and F. Liu, A polydopamine coated nanoscale FeS theranostic platform for the elimination of drug-resistant bacteria via photothermal-enhanced Fenton reaction, *Acta Biomater.*, 2022, **150**, 380–390.

12 J. Huo, Q. Jia, H. Huang, J. Zhang, P. Li, X. Dong and W. Huang, Emerging photothermal-derived multimodal synergistic therapy in combating bacterial infections, *Chem. Soc. Rev.*, 2021, **50**(15), 8762–8789.

13 X. Dong, J. Ye, Y. Chen, T. Tanziela, H. Jiang and X. Wang, Intelligent peptide-nanorods against drug-resistant bacterial infection and promote wound healing by mild-temperature photothermal therapy, *Chem. Eng. J.*, 2022, **432**, 134061.

14 A. Fabbri, A. Voza, A. Riccardi, S. Serra and F. D. Iaco, The pain management of trauma patients in the emergency department, *J. Clin. Med.*, 2023, **12**(9), 3289.

15 H. Güngör, B. Ciftci, S. Alver, B. E. Gölboyu, Y. Ozdenkaya and S. Tulgar, Modified thoracoabdominal nerve block through perichondrial approach (M-TAPA) vs local infiltration for pain management after laparoscopic cholecystectomy surgery: a randomized study, *J. Anesth.*, 2023, **37**(2), 254–260.

16 P. Mahon, C. Aitken, M. Veiga and S. Poitras, Time for action: Understanding health care professionals views on pain and pain Management in a Pediatric Hospital, *Pain Manag. Nurs.*, 2023, **24**(2), 171–179.

17 M. H. Huttunen, M. Paananen, J. Miettunen, E. Kalso and M. K. Marttinen, Multidisciplinary management of persistent pain in primary care—A systematic review, *Eur. J. Pain*, 2024, **28**, 886–900.

18 M. Salimi, S. Mosca, B. Gardner, F. Palombo, P. Matousek and N. Stone, Nanoparticle-mediated photothermal therapy limitation in clinical applications regarding pain management, *Nanomaterials*, 2022, **12**(6), 922.

19 J. Tesarz, C. Herpel, M. Meischner, A. Drusko, H. C. Friederich, H. Flor and J. Reichert, Effects of virtual reality on psychophysical measures of pain: superiority to imagination and nonimmersive conditions, *Pain*, 2024, **165**(4), 796–810.

20 K. R. Bagshaw, C. L. Hanenbaum, E. J. Carbone, K. W. Lo, C. T. Laurencin, J. Walker and L. S. Nair, Pain management via local anesthetics and responsive hydrogels, *Ther. Deliv.*, 2015, **6**(2), 165–176.

21 I. Perets, J. P. Walsh, B. H. Mu, L. C. Yuen, L. Ashberg, M. R. Battaglia and B. G. Domb, Intraoperative infiltration of liposomal bupivacaine vs bupivacaine hydrochloride for pain management in primary total hip arthroplasty: a prospective randomized trial, *J. Arthroplasty*, 2018, **33**(2), 441–446.

22 A. D. Kaye, C. Armstead-Williams, F. Hyatali, K. S. Cox, R. J. Kaye, L. K. Eng, M. A. Farooq Anwar, P. V. Patel, S. Patil and E. M. Cornett, Exparel for postoperative pain management: a comprehensive review, *Curr. Pain Headache Rep.*, 2020, **24**, 1–10.

23 P. Chen, J. Wang, X. Feng, K. Li, Q. Liu, L. Ji, H. Li, P. Sun, J. Li and B. Zhou, Bidirectionally Regulated Synthetic Ferrocene-based Aminal-linked Porous Organic Polymer Artificial Enzyme towards Photothermal-amplified Synergistic Antibacterial and Wound Healing Therapy, *Polym. Test.*, 2024, **22**, 108466.

24 Z. Xu, L. Hu, J. Ming, X. Cui, M. Zhang, J. Dou, W. Zhang and B. Zhou, Self-gated porous organic polymer as drug delivery system for pH stimuli-responsive controlled Quercetin release, *Microporous Mesoporous Mater.*, 2020, **15**(303), 110259.

25 Z. Zhang, L. Shi, L. Chu, P. Chen, P. Sun, Z. Chen, L. Wei and B. Zhou, Crown ether-based porous organic polymer encapsulated $Ag_2[Fe(CN)_5NO]$ composite towards ultra-low dose efficient sterilization and wound healing application, *Mater. Today Chem.*, 2023, **34**, 101794.

26 H. Lou, H. Fang, T. Wang, D. Wang, Q. Han, W. Zhou, Y. Song, W. Tan and B. Zhou, Biodegradable porous polymeric drug with pH-stimuli-responsive delivery capacity for combined cancer therapy, *ACS Appl. Polym. Mater.*, 2021, **8**(1), 714–724.

27 Q. Yue, J. Yu, Q. Zhu, D. Xu, M. Wang, J. Bai, N. Wang, W. Bian and B. Zhou, Polyrotaxanated covalent organic frameworks based on β-cyclodextrin towards high-efficiency synergistic inactivation of bacterial pathogens, *Chem. Eng. J.*, 2024, **486**, 150345.

28 M. G. Mohamed, A. F. EL-Mahdy, M. G. Kotp and S. W. Kuo, Advances in porous organic polymers: syntheses, structures, and diverse applications, *Mater. Adv.*, 2022, **3**(2), 707–733.

29 Y. Zhu, P. Xu, X. Zhang and D. Wu, Emerging porous organic polymers for biomedical applications, *Chem. Soc. Rev.*, 2022, **51**(4), 1377–1414.

30 S. Wang, J. Zhang, L. Chu, C. Miao, Z. Pan, Y. Qiao, Z. Wang and B. Zhou, Crown-ether threaded covalent organic polyrotaxane framework (COPF) towards synergistic crown/$Zn^{2+}$/photothermal/photodynamic antibacterial and infected wound healing therapy, *Biomater. Adv.*, 2024, **26**, 213814.

31 Z. Pan, Y. Fu, C. Peng, S. Zhu, F. Peng, Q. Liu and B. Zhou, Triazine-porphyrin-based aminal linked porous organic polymer as self-enhanced photo/enzyme synergistic antibacterial agent for wound healing, *Microporous Mesoporous Mater.*, 2024, **365**, 112881.

32 B. Zhou, L. Liu, P. Cai, G. Zeng, X. Li, Z. Wen and L. Chen, Ferrocene-based porous organic polymer derived high-performance electrocatalysts for oxygen reduction, *J. Mater. Chem. A*, 2017, **5**(42), 22163–22169.

33 N. Singh, S. Son, J. An, I. Kim, M. Choi, N. Kong, W. Tao and J. S. Kim, Nanoscale porous organic polymers for drug delivery and advanced cancer theranostics, *Chem. Soc. Rev.*, 2021, **50**(23), 12883–12896.

34 L. Wang, L. Shi, T. Guo, J. Yuan, B. Zhou and J. Zhang, Near-infrared active ferrocenyl porous organic polymer with photothermal enhanced enzymatic activity for combination antibacterial application, *RSC Adv.*, 2023, **13**(38), 26445–26454.

35 H. Luo, T. Huang, X. Li, J. Wang, T. Lv, W. Tan, F. Gao, J. Zhang and B. Zhou, Synergistic antibacterial and wound-healing applications of an imidazole-based porous organic polymer encapsulated silver nanoparticles composite, *Microporous Mesoporous Mater.*, 2022, **337**, 111925.

36 B. Zhou, F. Yan, X. Li, J. Zhou and W. Zhang, An interpenetrating porous organic polymer as a precursor for FeP/$Fe_2P$-embedded porous carbon toward a pH-universal ORR catalyst, *ChemSusChem*, 2019, **21**(4), 915–923.

37 H. Luo, X. Chen, T. Huang, W. Kang, X. Li, Z. Jiang, L. Pang, J. Bai, W. Tan, J. Li and B. Zhou, In situ simultaneously integrating Co-NC sites and Co9S8 nanoparticles into N, S-doped porous carbon as trifunctional electrocatalysts for Zn–air batteries driving water splitting, *J. Environ. Chem. Eng.*, 2022, **10**(2), 107203.

38 M. Mirhosseini and M. Afzali, Investigation into the antibacterial behavior of suspensions of magnesium oxide nanoparticles in combination with nisin and heat against Escherichia coli and Staphylococcus aureus in milk, *Food Control*, 2016, **68**, 208–215.

39 C. Mutalik, G. Okoro, D. I. Krisnawati, A. Jazidie, E. Q. Rahmawati, D. Rahayu, W. T. Hsu and T. R. Kuo, Copper sulfide with morphology-dependent photodynamic and photothermal antibacterial activities, *J. Colloid Interface Sci.*, 2022, **607**, 1825–1835.

40 E. Pakdel, J. Sharp, S. Kashi, W. Bai, M. P. Gashti and X. Wang, Antibacterial superhydrophobic cotton fabric with photothermal, self-cleaning, and ultraviolet protection functionalities, *ACS Appl. Mater. Interfaces*, 2023, **15**(28), 34031–34043.

41 H. Zhang, Q. Li, X. Qi, Y. Li, H. Ma, M. Grinholc, J. Nakonieczna, B. Yu, X. Wang and L. Zhang, Iron-blocking antibacterial therapy with cationic heme-mimetic gallium porphyrin photosensitizer for combating antibiotic resistance and enhancing photodynamic antibacterial activity, *Chem. Eng. J.*, 2023, **451**, 138261.

42 X. Duan, Y. Xu, Z. Zhang, X. Ma, C. Wang, W. Ma, F. Jia, X. Pan, Y. Liu, Y. Zhao and Q. Li, Piezoelectrically-activated antibacterial catheter for prevention of urinary tract infections in an on-demand manner, *Mater. Today Bio*, 2024, **11**, 101089.

43 C. Liu, W. Du, L. Jiang, Y. Li, C. Liu and X. Jian, Enhanced antibacterial and adhesive properties of chitosan/gelatin hydrogel containing berberine hydrochloride and prepolymerized gallic acid exhibiting aggregation-induced emission, *Polym. Eng. Sci.*, 2023, **63**, 2596–2612.

44 Q. Song, D. Xu, W. Bian, J. Wang, G. Peng, M. Sun, N. Wang and B. Zhou, Cationic Cu (I)-covalent organic framework as self-enhanced synergetic Photothermal/Phtodynamic/Cationic/Enzymatic antibacterial agent, *React. Funct. Polym.*, 2023, **192**, 105692.

45 P. Chen, R. Ze, Z. Zhang, K. Lu, L. Wei and B. Zhou, Composite porphyrin-based conjugated microporous polymer/graphene oxide capable of photo-triggered combinational antibacterial therapy and wound healing, *Biomater. Adv.*, 2023, **154**, 213662.

46 W. Guo, J. Hao, M. Wang, T. Huang, C. Miao, L. Yin, H. Ji, F. Gao and B. Zhou, Polypyrrole hydrogel with near-infrared light-driven nitric oxide release and photothermal activities for rapid synergistic sterilization and infected wound therapy, *Colloids Surf. A Physicochem. Eng. Asp.*, 2023, **677**, 132411.

47 S. Bhusari, J. Kim, K. Polizzi, S. Sankaran and A. Del Campo, Encapsulation of bacteria in bilayer Pluronic thin film hydrogels: a safe format for engineered living materials, *Biomater. Adv.*, 2023, **145**, 213240.

48 X. Cai, L. Gao, J. Wang and D. Li, MOF-integrated hierarchical composite fiber for efficient daytime radiative cooling and antibacterial protective textiles, *ACS Appl. Mater. Interfaces*, 2023, **15**(6), 8537–8545.

49 R. Yu, H. Chen, J. He, Z. Zhang, J. Zhou, Q. Zheng, Z. Fu, C. Lu, Z. Lin, F. Caruso and X. Zhang, Engineering antimicrobial metal–phenolic network nanoparticles with high biocompatibility for wound healing, *Adv. Mater.*, 2024, **36**(6), 2307680.